






Article

Dynamic Control of Airy Beams Using Real-Time Phase-Amplitude Encoding on a Spatial Light Modulator

Alpgiray Keskin ¹, Gamze Kaya ², Necati Kaya ^{3,*}, James Strohaber ⁴, Alexandre A. Kolomenskii ⁵
and Hans A. Schuessler ⁵

¹ Energy Technology Program, School of Graduate Studies, Canakkale Onsekiz Mart University, Canakkale 17020, Türkiye; alpgiray_keskin@yahoo.com

² Department of Electric and Energy, Vocational School of Technical Sciences, Canakkale Onsekiz Mart University, Canakkale 17020, Türkiye; gamzekaya@comu.edu.tr

³ Department of Material Science and Engineering, Faculty of Engineering, Canakkale Onsekiz Mart University, Canakkale 17020, Türkiye

⁴ Department of Physics, Florida A & M University, Tallahassee, FL 32307, USA; james.strohaber@famu.edu

⁵ Department of Physics & Astronomy, Texas A & M University, College Station, TX 77843, USA; alexandr@physics.tamu.edu (A.A.K.); schuessler@physics.tamu.edu (H.A.S.)

* Correspondence: necatikaya@comu.edu.tr

Abstract: Airy beams showing curved paths have found extensive applications in fields such as optical trapping, biomedical analysis, and material processing. Despite their utility, dynamic control of Airy beams poses a significant challenge. This work investigates the experimental realization of dynamic steering of Airy beams by utilizing computer-generated holograms with phase-amplitude encoding on a phase-only spatial light modulator (SLM). We successfully generated and controlled Airy beams by imposing dynamic phase masks that manipulated both the phase and amplitude of the field, which sets our approach apart from conventional methods with only phase manipulation. By directly encoding in situ such a hologram and transferring it to an SLM, we are able to control the initial position and rotational orientation of Airy beams without relying on mechanical movement or traditional optical setups involving lenses and apertures. Generating Airy beams in any initial position and rotational direction is anticipated to significantly impact applications such as optical trapping, optical communication, and biomedical imaging by providing a flexible platform for dynamic Airy beam manipulation.

Keywords: optical airy beam; spatial light modulator; computer-generated hologram; phase-amplitude encoding



Citation: Keskin, A.; Kaya, G.; Kaya, N.; Strohaber, J.; Kolomenskii, A.A.; Schuessler, H.A. Dynamic Control of Airy Beams Using Real-Time Phase-Amplitude Encoding on a Spatial Light Modulator. *Optics* **2024**, *5*, 581–594. <https://doi.org/10.3390/opt5040043>

Academic Editor: Jieyun Wu

Received: 15 October 2024

Revised: 21 November 2024

Accepted: 29 November 2024

Published: 3 December 2024



Copyright: © 2024 by the authors. Licensee MDPI, Basel, Switzerland. This article is an open access article distributed under the terms and conditions of the Creative Commons Attribution (CC BY) license (<https://creativecommons.org/licenses/by/4.0/>).

1. Introduction

Diffraction is a common phenomenon in optics, affecting most conventional light waves. Researchers have been investigating ways to create non-diffracting beams for some time. In 1987, Durnin made a significant breakthrough by finding an exact solution to the Maxwell wave equation using the zero-order Bessel function [1]. This solution demonstrated that the resulting wave exhibited non-diffraction characteristics and, in addition, that it could be realized using simple and conventional optical elements. This discovery marked the formal introduction of the notion of diffraction-free beams [2]. Subsequent research uncovered other types of non-diffracting beams, extending beyond Bessel beams propagating in straight lines and encompassed also Airy beams that showed curved trajectories. As early as 1979, Berry and Balazs predicted the existence of Airy beams, describing a single Airy wave packet as the only non-diffracting solution to the Schrödinger equation [3]. Unsatisfactorily, the original Airy function had infinite energy, which is unrealistic. To overcome this limitation, Siviloglou et al. conducted an in-depth investigation of the solution and introduced an exponential decay function as an additional multiplier to the

original Airy function [4]. This approach, similar to the technique used to create Bessel beams, effectively mitigated the problem of infinite energy. The modified Airy function still satisfied the requirements of the Schrödinger equation. The first practical implementation of a truncated Airy beam was accomplished using a spatial light modulator, which brought Airy beams into the realm of experimentally observable optical beams [5]. Subsequent extensive research revealed that Airy beams, in addition to their non-diffracting nature, possessed remarkable properties of self-acceleration and self-healing, resembling that of Bessel beams [6–8]. These distinctive characteristics of Airy beams have captured the interest of researchers and opened up numerous potential applications in the fields of modern optics and photonics. Various studies have verified the diverse applications of Airy beams, including their utilization in optical bullets [9–11], optical bottle beam formations [12], optical routing [13], electron acceleration [14], light sheet microscopy [15–17], tomographic measurements [18], plasma channels [19], acoustics [20], and particle clearing and optical manipulation of particles [21,22]. Airy beams have also been studied in the context of matter waves [23], spin waves [24], water waves [25], and light-induced waveguiding [26]. Furthermore, owing to their resilience in disturbed environments and their ability to self-heal, Airy beams have found applications in microscopic examinations of biological cells, atmospheric optical filamentation, and optical communication systems [8]. In fields such as microfluidic engineering and cell biology, Airy beams offer the capability to manipulate charged microscopic particles along curved and intricate paths [15]. In addition, investigated possible uses of Airy beams include Airy acoustic sheet rotating tweezers [27], finite asymmetric exotic beam acoustics [28], optical tweezing, imaging and microscopy, multiple photon excitation [29] and attenuation compensation to obtain imaging at greater depths within biological samples [30,31]. The self-accelerating and diffraction-free properties of the Airy wave packet and the generation of two-dimensional, circular Airy waves with abruptly autofocusing beams [32] find applications in micro processing and medical laser microsurgery and treatment [33].

To date, research on Airy beams has primarily focused on the linear optical regime. Typically, they are generated using moderate laser intensities with cylindrical lenses [34,35] or through binary phase patterns with liquid crystals [36]. However, integrating nonlinear optical processes into Airy beams enhances their functionality, for example, by broadening their wavelength spectrum [37,38]. Despite these advancements, a major challenge in the study of Airy beams is the active modulation and multiplexing of their propagation characteristics, such as controlling the acceleration direction and trajectory. While metasurfaces have been employed to adjust the propagation path of Airy beams [39], they exhibit low nonlinear transformation efficiency for generating nonlinear Airy beams. An alternative platform for dynamically controlling nonlinear Airy beams is 1D or 2D nonlinear photonic crystals (NPCs) [40–42]. However, these platforms often face strict operational requirements and are limited in flexibility and working frequency ranges. As a result, there is a pressing need for the development of a universal approach that enables the efficient generation and flexible manipulation of Airy beams.

In this study, we generated computer-controlled dynamic Airy holograms using phase-amplitude encoding on a phase-grating structure, resulting in experimentally generated Airy beams with changeable curved directions. Rather than moving optical components (such as lenses and apertures) for manipulation of an Airy beam, we modified the hologram in situ to change the phase-amplitude mask in real time, allowing us to control the direction of the Airy beam as needed. To create an Airy beam using a reflective phase-only spatial light modulator (SLM), the desired phase-amplitude pattern is first calculated using analytical methods that take into account the SLM calibration, the optimized grating period, and modulation depth. Then, the phase-amplitude pattern is uploaded to the SLM, which imposes the required phase and amplitude modulation onto the incident laser beam. Unlike other methods that use cubic phase modulation and then perform Fourier transform with a focusing lens [5,13], we form an Airy beam directly with the SLM. In addition, we explicitly present the correction procedure that enables exact reproduction of an Airy beam

in the first diffraction order. With this approach, the parameters of the Airy beams can be easily changed by controlling the phase and amplitude pattern set on the SLM, thus offering a flexible method to study propagation characteristics of the Airy beams, such as their acceleration direction and trajectory. This technique can be applied for different light wavelengths and for a wide dynamic range of laser intensities and is expected to have a broad impact on applications such as optical trapping, optical communication, biomedical imaging, etc., by offering a versatile platform for dynamic control of Airy beams. This paper is organized as follows: (1) introduction, (2) modeling aspects, (3) experimental methods and results, and (4) conclusions.

2. Modelling Aspects

2.1. Analytical Framework for Airy Beams

The Airy wave function first considered by Berry and Balazs [3] is a solution of the field-free Schrödinger equation. A similar equation has also been used to describe the diffraction of propagating waves within the paraxial approximation. The field distribution of a finite-power Airy beam with an exponential limiting factor at the input $z = 0$ plane can be expressed as

$$E(x, y, z = 0) \propto \text{Ai}\left(\frac{x}{r_0}\right) \text{Ai}\left(\frac{y}{r_0}\right) \exp\left[a\left(\frac{x+y}{r_0}\right)\right] \quad (1)$$

where Ai is the Airy function, r_0 is a characteristic transverse scaling factor, and a is a small positive constant to ensure energy confinement of the beam. We note that the Fourier transform of Equation (1) contains a Gaussian distribution multiplied by a cubic phase term, the latter being the inherent property of the Airy function [4]. The propagating Airy beam with the boundary condition of Equation (1) can be presented by the following expression for the field [5,19,43]:

$$E \propto \text{Ai}(\xi) \text{Ai}(\eta) \exp\left[a\left(\frac{x+y}{r_0}\right) - a\zeta^2 - i\left(\frac{\zeta^3}{12} - \frac{a^2\zeta}{2} - \frac{(x+y)\zeta}{2r_0}\right)\right]. \quad (2)$$

Here $\xi = x/r_0 - \zeta^2/4 + ia\zeta$ and $\eta = y/r_0 - \zeta^2/4 + ia\zeta$, and $\zeta = z/(kr_0^2)$ is the normalized propagation distance along the z -axis, $k = 2\pi/\lambda$ is the wave number, and λ is the wavelength of the wave. The intensity profile of the propagating Airy beam can then be described by the modulus-squared of the field:

$$I(x, y, z) \propto |E(x, y, z)|^2 \propto \left| \text{Ai}^2(\xi) \text{Ai}^2(\eta) \exp\left[2a\left(\frac{x+y}{r_0}\right) - 2a\zeta^2\right] \right|. \quad (3)$$

The propagation length of this wave, at which the intensity drops by a factor e^{-2} can be estimated as $L \approx kr_0^2/\sqrt{a}$ [19], and for small values of the parameter a , the trajectory follows a parabolic curve in three-dimensional space: $\{x = y = z^2/(4k^2r_0^3)\}$.

2.2. Phase-Amplitude Pattern Design

We utilized MATLAB to generate a hologram code for manipulation of Airy beam profiles, concentrating mainly on the rotation of the amplitude distribution of the beam and the corresponding adjustment of the phase mask. The methodology consists of several key steps, which are detailed below. First, we set up the Airy beam spatial domain and calculated its amplitude using Airy functions. A 2D Airy beam is separable into the product of two 1D Airy functions for the x and y axes at $z = 0$ according to Equation (1). Second, the beam amplitude is normalized, i.e., the amplitude distribution $M(x, y) = |E(x, y, z = 0)|/\max|E(x, y, z = 0)|$ is used to ensure a consistent maximum value across the grid, which is crucial for comparing different beam configurations or analyzing the intensity distribution. It was shown [44,45] that to obtain a beam with an arbitrary complex amplitude distribution, $M(x, y) \exp[i\Phi(x, y)]$, one can achieve this

approximately with a phase-only mask $\Psi(x, y)$ on the SLM by imposing an amplitude modulation of the phase structure and in addition by applying a periodic phase variation of a grating:

$$\Psi(x, y) = \text{mod}[0.5(M(x, y)\Phi(x, y) + \Phi_{gr}(x, y)) + \pi, 2\pi]. \quad (4)$$

Here, we use a sawtooth-shaped grating profile $\Phi_{gr}(x, y) = \pi MD \text{sawtooth}(2\pi x/\Lambda)$ (the MATLAB sawtooth function with the limits $[-1, 1]$ was employed), the modulation depth was set to $MD = 1$, Λ is the grating period, and the modulo function mod [44,45] assures that the imposed phase changes within the limits $[0, 2\pi]$. For the case of a real number amplitude as in Equation (1), which can have positive or negative sign, the phase has the values $\Phi(x, y) = 0$ for $E(x, y) \geq 0$ and $\Phi(x, y) = \pi$ for $E(x, y) < 0$. For this case, amplitude distribution in the first diffraction order is as follows [45],

$$A_1(x, y) \propto R_0 \text{sinc}\{\pi[1 - M(x, y)] \exp[i(2\pi x/\Lambda + \Phi_{\text{shift}})]\} \quad (5)$$

where $R_0 \approx 1$ is the amplitude reflection coefficient of the SLM with a zero phase imposed, the function $\text{sinc}(u) = \sin(u)/u$ for $u \neq 0$ and 1 for $u = 0$, and the term $\Phi_{\text{shift}} = (\pi/2)[1 + \text{sign}(E(x, y))]$ is used to take into account the sign of the local field [45,46]. The intensity I of the beam is proportional to the square of the amplitude modulus; see Equation (3). This corresponds to the physical energy distribution of the beam in space, a key metric in optical beam analysis.

To obtain an Airy beam with an orientation rotated by a specified angle θ , the following rotation matrix is applied:

$$\begin{pmatrix} x' \\ y' \end{pmatrix} = \begin{pmatrix} \cos \theta & -\sin \theta \\ \sin \theta & \cos \theta \end{pmatrix} \begin{pmatrix} x \\ y \end{pmatrix}. \quad (6)$$

This matrix rotates the coordinates by an angle θ , which transforms the grid onto new rotated coordinates. We note that the rotation of the system of coordinates of Equation (6) by angle θ corresponds to the rotation of the phase mask in this system of coordinates by angle $(-\theta)$, and the rotation of the phase mask by angle θ corresponds to the rotation of the beam on the target (in our experiment the detection camera) by $(-\theta)$. After rotation, the amplitude is interpolated on the rotated grid. This interpolation is necessary because the rotation does not map the coordinates directly onto a uniform grid of the SLM.

The rotation leads to the following substitution in Equations (4) and (5),

$$M(x, y) \rightarrow M[x'(x, y), y'(x, y)] = M_R(x, y, \theta) \quad (7)$$

where we have introduced a new function of x, y , namely $M_R(x, y, \theta)$, which corresponds to a rotated Airy beam distribution, leading also to a changed orientation of the beam trajectory. As follows from Equation (5), the amplitude in the first diffraction order is then described by the following formula: $|A_{1,R}(x, y)| = \text{sinc}[\pi(1 - M_R(x, y, \theta))]$, which is the obtained approximation that is, however, not exactly equal to the desired amplitude modulation $M_R(x, y, \theta)$. To correct for this discrepancy, instead of $M_R(x, y, \theta)$ we introduce in Equation (7) a modified function,

$$M_{R,corr}(x, y, \theta) = K[M_R(x, y, \theta)]M_R(x, y, \theta) \quad (8)$$

with the amplitude correction function $K(u)$ depending only on the properties of the sinc (u) function and its argument. This function $K(u)$ is defined by the equation:

$$\text{sinc}[\pi(1 - K(u)u)] = u \text{ for } 0 \leq u \leq 1. \quad (9)$$

The function $K(u)$ calculated for $0 \leq u \leq 1$ is depicted in Figure 1a, showing that the value of the correction function for a given amplitude is determined by the value of the

amplitude itself. Then, the amplitude of the corrected output in the first diffraction order is described by the formula,

$$|A_{1,R,corr}(x, y)| = \sin c[\pi(1 - M_{R,corr}(x, y, \theta))] \quad (10)$$

with $M_{R,corr}(x, y, \theta)$ defined by Equation (8).

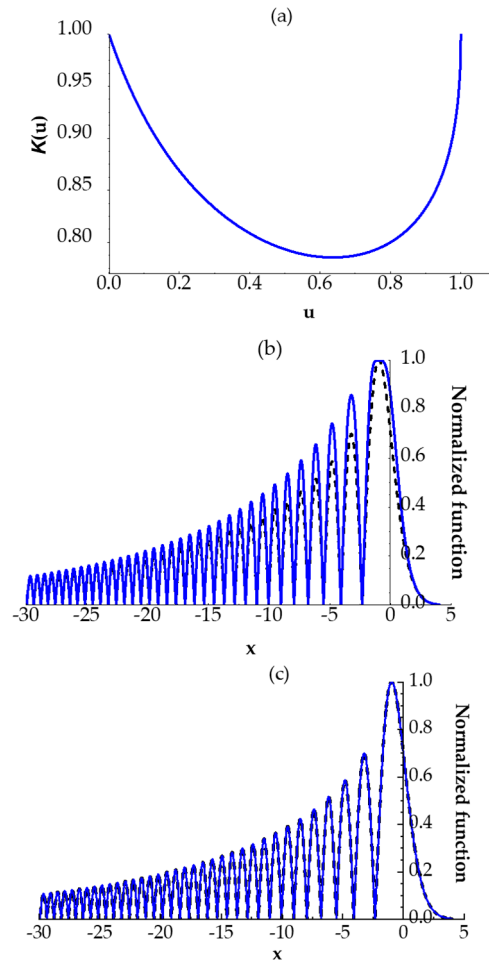


Figure 1. Approximation of a truncated Airy function by the expected distribution in the first diffraction order: (a) amplitude correction function, (b) the input Airy function (blue) and the uncorrected output distribution in the first diffraction order (black, dashed), (c) the input Airy function (blue) and the corrected output distribution in the first diffraction order (black, dashed), showing very close agreement.

2.3. Simulation Results

The calculations show that before the correction the ratio of the desired modulation function $M_R(x, y, \theta)$ and the obtained approximation $|A_{1,R}(x, y)|$ for all significant x, y points with $M_R(x, y, \theta) > 0.1$ varies from ~ 0.78 to 1, i.e., the approximation can deviate by about 25%. With the correction, the ratio of $M_R(x, y, \theta)$ and $|A_{1,R,corr}(x, y)|$ varies within a much narrower interval of less than 0.15%, mostly determined by the accuracy of the calculation. This is illustrated by the results for the calculated modulation function presented in Figure 1b,c for $\theta = 0$, $a = 0.05$, and $y = -0.968$ (the y value for the Airy function maxima along the x -axis). It can be seen that by applying the outlined correction, much better accuracy of the generated Airy beam can be obtained.

Consequently, the described approach allows for precise control over the characteristics of the optical beam profiles, providing an effective way for manipulating Airy beams

in practical applications. We visualize the amplitude, intensity, and phase-amplitude hologram using 2D surface plots in Figure 2.

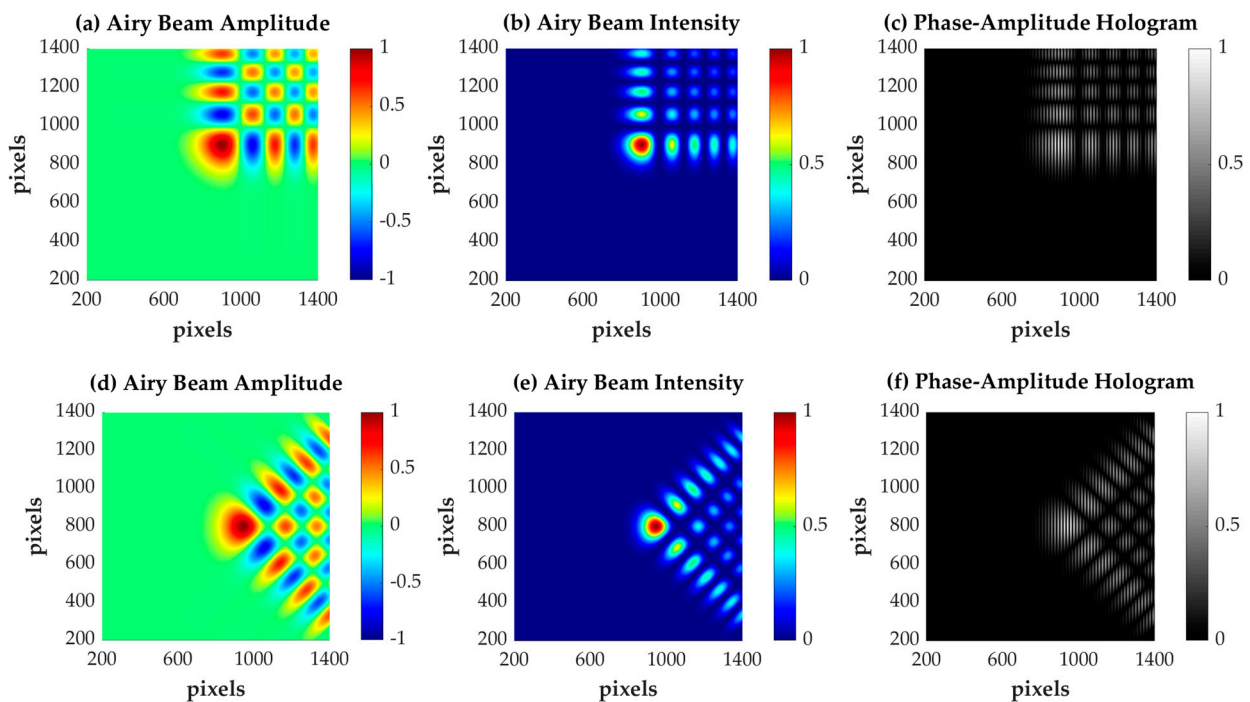


Figure 2. The amplitude of the Airy beam is computed as the product of two 1D Airy functions, one along each axis (x and y); see Equation (1) with $x \rightarrow -x$, and $y \rightarrow -y$. To rotate the beam, the rotation matrix is applied to the grid coordinates, followed by interpolation. The resultant Airy beam amplitude and intensity, as well as the corresponding phase-amplitude hologram are presented: (a) Airy beam amplitude distribution. (b) Airy beam intensity distribution. (c) The phase-amplitude hologram corresponding to the unrotated Airy beam. (d,e) present the Airy beam amplitude and intensity distributions after applying rotation of $\theta = -45^\circ$. (f) depicts the phase-amplitude hologram for the rotated beam.

3. Experimental Methods and Results

3.1. Calibration of the SLM for Phase Modulation

In our experiment, we utilized an SLM (EXULUS-HD1) that integrates an LCoS panel with a resolution of 1920×1080 pixels, an active area of $12.5 \text{ mm} \times 7.1 \text{ mm}$, and a pixel pitch of $6.4 \mu\text{m}$. Because the modal structure of Airy beams requires proper amplitude and phase modulation, appropriate calibration of the SLM is crucial for obtaining accurate and reliable results, making it an essential step for high-precision applications. We employed a continuous wave He-Ne laser with a wavelength of 632.8 nm and a beam diameter of 0.65 mm (TEM_{00} , $1/e^2$). Note that the phase shift induced by the SLM is wavelength-dependent and will affect the device's phase calibration. The phase calibration was determined by measuring the SLM reflectivity (the ratio of the values of the reflected and incident light powers) for a set of grayscale values imposed onto the LCoS panel of the SLM. The reflected laser power was measured by setting up a Michelson interferometer [47]. The configuration of the interferometer is fixed, so the phase changes produced by varying the grayscale values between 0 and 255 in steps of three on the SLM in one of the arms resulted in variations in the laser output power. An example grayscale and the experimental setup are shown in Figure 3.

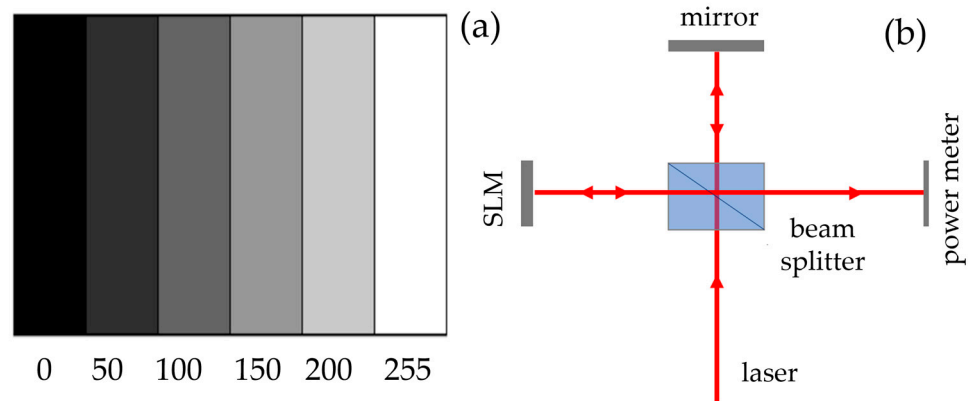


Figure 3. (a) Six grayscale values as an example of the 0–255 grayscale used in the calibration process and (b) the Michelson interferometer experimental setup used for the SLM calibration.

A uniform grayscale image on the SLM assigns to each pixel a grayscale value, starting from black (grayscale value 0) to white (grayscale value 255), as shown in Figure 3a. With an SLM of high reflectivity (assumed to be 1), the initial power of the laser beam P_0 , and the reflectivity of the beam splitter R , the power of each of the two sub-beams arriving at the photodetector is $P_0(1 - R)R$. Then, considering the phase shift φ produced by the SLM for monochromatic laser light, the total power measured by the power meter is found to be:

$$P = P_0(1 - R)R |1 + e^{i\varphi}|^2 = P_0(1 - R)R 2(1 + \cos(\varphi)). \tag{11}$$

Here, the phase difference between the two fixed arms is φ . For $R = 0.5$,

$$P = P_0 \cos^2(\varphi/2). \tag{12}$$

As the grayscale values (and the phase too) were changed, the total laser power was measured by the power meter (Thorlabs, PM100USB, S120C). The recorded data are shown in Figure 4a. They have been fitted by the theoretically expected formula of Equation (12) (solid blue curve). From this fit, the phase modulation as a function of grayscale value was determined using relation $\varphi = 2\arccos(\sqrt{P/P_0})$ and is shown in Figure 4b. The relationship between the phase modulation φ and the grayscale value χ is well approximated by a linear function $\varphi = 0.124 + 0.008\chi$, which corresponds to 0.008π radians per grayscale value in addition to an offset phase of 0.124π radians. Notably, the maximum phase modulation reached approximately 2π radians when the grayscale value χ was equal to 234.

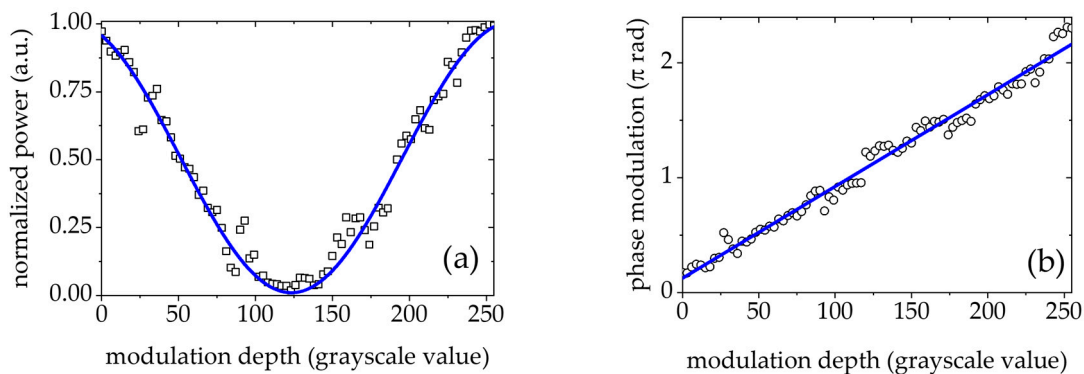


Figure 4. (a) The power output measured in a Michelson interferometer as a function of the grayscale values. The data points of the measured output power are represented by black open squares, while the solid blue line shows the theoretical fit with Equation (12). (b) Phase modulation retrieved from the data and the theoretical fit.

3.2. Diffraction Efficiency Optimization

The diffraction efficiency resulting from the phase pattern displayed on the SLM was optimized over the grating period (determined by the number of pixels in a period) and the modulation depth (grayscale values). The experimental arrangement for this optimization process is shown in Figure 5.

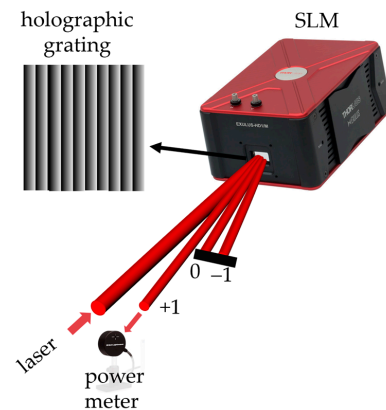


Figure 5. Experimental setup for measuring diffracted laser beam intensities using a spatial light modulator (SLM). A laser beam is incident on the SLM, displaying a holographic grating pattern, which results in multiple diffraction orders (0, +1, −1). To measure the first-order diffraction efficiency of the grating as a function of the modulation depth (grayscale values) using different grating periods, a power meter is placed in the path of the first-diffraction-order beam.

The gratings with N steps were generated by a computer. The first-order diffraction efficiency was measured for the modulation depth (MD) and different number of pixels (NP) in a grating period. Top and side views of the grating phase structures on the SLM with grating period (with certain number of pixels, NP) and grayscale (modulation depth, MD) are shown in Figure 6. In this figure, grating structures were exaggerated to better visualize the parameters of the grating. In Figure 7a, we depicted the grating efficiency as a function of the modulation depth, which was determined by calculating the ratio of the power in the first diffraction order to the power in the zero order. A total of ten data sets were obtained, with each set representing a distinct grating period. The grating period is indicated by the number of pixels (NP) employed, assuming that each pixel corresponded to a pitch of $6.4 \mu\text{m}$. All data sets showed a peak at a grayscale value of ~ 234 , which corresponds to a phase shift of $\sim 2\pi$ radian, where the maximum peak values of efficiencies are obtained in the measurements (see Figure 7a). In Figure 7b, the efficiencies observed at the peak values (grayscale value of 234) for different grating periods are plotted, showing that the highest diffraction efficiency is achieved for a grating period of eight pixels. Notably, as the number of steps increased or decreased from this optimal value, the diffraction efficiency demonstrated a gradual decrease.

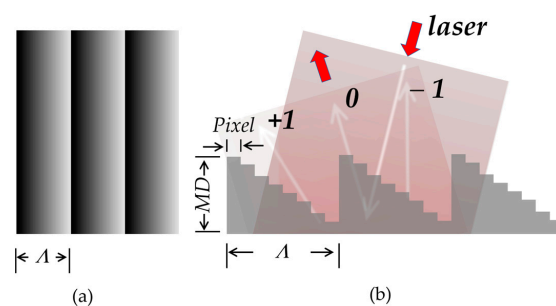


Figure 6. A blazed phase grating having modulation depth (MD) and grating period (Λ) displayed on the SLM (a) top and (b) side views. The grating phase structures and features are exaggerated for better visualization.

From Figure 7, it is suggested that for achieving maximum efficiency, a modulation depth around a grayscale value of 234 and a grating period of eight pixels are optimal. There is a trade-off between NP and efficiency; smaller or larger NP values result in reduced efficiency. This also results in a trade-off between spatial resolution (determined by NP) and the efficiency of diffraction. For applications requiring high diffraction efficiency, setting the SLM parameters close to these optimal values would be beneficial. Adjusting the grating period and modulation depth can fine-tune the performance of the setup for specific needs.

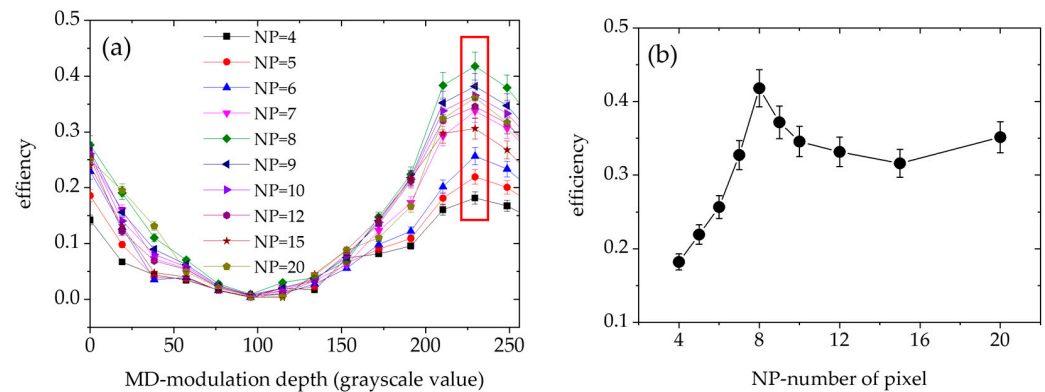


Figure 7. (a) Diffraction efficiency of the grating as a function of modulation depth (grayscale value) for different grating periods (NP—number of pixels). The efficiency is determined by the power ratio of the first diffraction order to the zero order. Maxima of efficiencies (in a red box) are achieved at a grayscale value of 234, corresponding to a phase modulation depth of 2π . (b) Diffraction efficiencies at a grayscale value of 234 as a function of the grating period (NP), showing the maximum value at a period of eight pixels.

3.3. Airy Beam Generation and Control

Figure 8 illustrates the experimental setup, and the operation of the optical system can be summarized as follows. A He-Ne laser beam with a wavelength of 632.8 nm first passes through a spatial filter, which removes higher modes and disturbances in the spatial profile and expands the Gaussian beam diameter by a factor of eight. This resulted in a final beam diameter of 5.2 mm (TEM_{00} , $1/e^2$) to utilize the panel's active area (which measures 12.5 mm \times 7.1 mm) and to accommodate the pixel pitch of 6.4 μm . The expanded beam is then sent through a polarizer to ensure that the polarization direction of the incident beam is aligned with the long axis of the liquid crystal molecules. The beam subsequently reaches the SLM device at an incidence angle of approximately 5° . The SLM modulates the incident beam with the encoded phase-amplitude mask. Ultimately, a 2D Airy beam obtained in the +1 diffraction order is captured by a camera (Basler ace2, a2A 1920).

In many applications, precise control over the propagation trajectory of an Airy beam is necessary to achieve the desired effect. By manipulating the central position of the mask shown in Figure 2, the original position of the generated Airy beam can be adjusted so that the trajectory of the Airy beam is controlled. Experimental 2D holographic Airy beam images taken with a CCD camera are presented in Figure 9a–d, which were obtained with the holograms located at the center and shifted by 40, 80, and 120 pixels along the x and y directions on the SLM, respectively. The shifts in the hologram result in predictable changes in the beam position and its intensity profile, demonstrating the flexibility of SLMs in beam-shaping applications.

The inherent modulation of the Airy beam causes them to self-bend during propagation. It is noted that the profiles of the observed Airy beams produce the expected Airy beam structure, thus confirming the validity of the proposed generation method. Figure 10 illustrates corresponding intensity distributions of Airy beam at (a) the central position and (b) 40, (c) 80, and (d) 120 pixels shifted along the x and y direction for different phase masks. The generated Airy beams were measured at about 20 cm away from the SLM. As the phase mask is shifted, the peak intensity in each distribution moves progressively to the

left and down. The results demonstrate how shifting the phase mask influences positioning of the beam in a controlled manner.

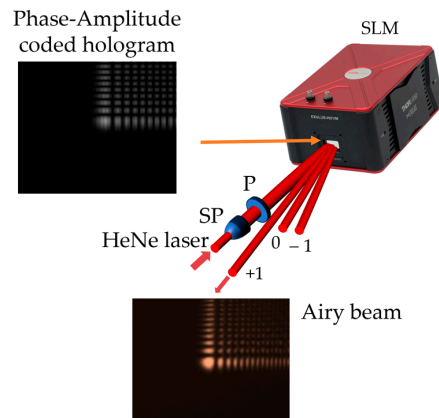


Figure 8. The experimental setup for generating Airy beams using a spatial light modulator (SLM). A He-Ne laser beam passes through a spatial filter (SP) and a polarizer (P) and is incident on the SLM. A phase-amplitude encoded hologram displayed on the SLM modulates the laser beam, producing diffraction orders (0, +1, −1). The first-order diffraction (+1) was selected to form the Airy beam shown in the bottom image.

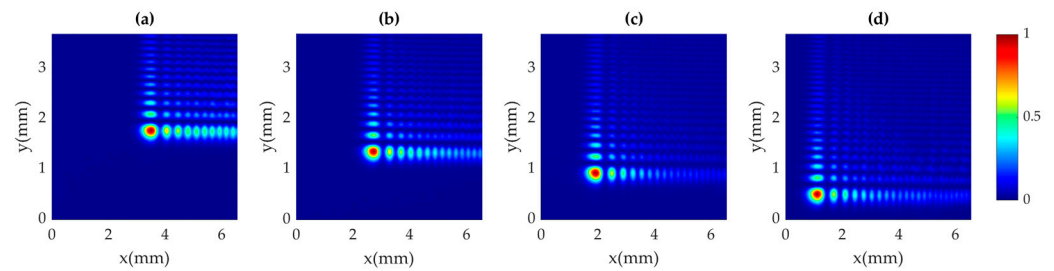


Figure 9. Experimental results of optical Airy beams generated using displaced holographic phase masks on the SLM. Each figure shows results captured by a CCD camera for the hologram: (a) positioned at the center, (b) shifted by 40 pixels along the x-axis, (c) shifted by 80 pixels along the x-axis, and (d) shifted by 120 pixels along the x-axis on the SLM.

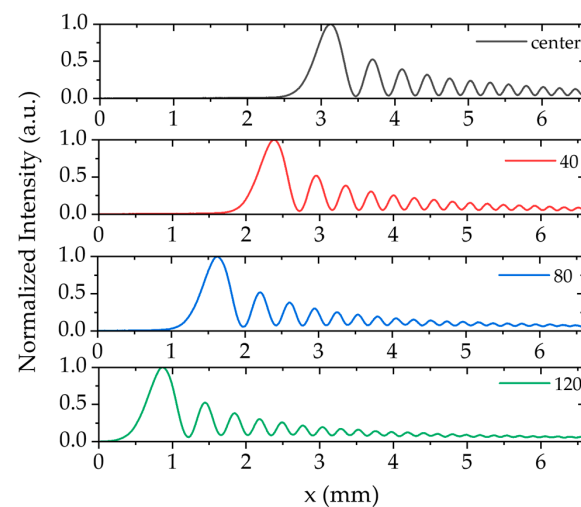


Figure 10. Intensity distributions of an Airy beam along the crests of the peaks for phase masks. The beam is positioned (from the top to the bottom) in the center and then shifted to the left by 40 pixels, 80 pixels, or 120 pixels along the x-direction.

Figure 11 displays intensity distributions for different orientations of optical Airy beams, visualized for both positive (from 0° to 180° , left column) and negative (from 0° to -180° , right column) angular displacements. We note that by changing the Airy pattern orientation, the direction of acceleration also changes, typically towards the main lobe of the beam, which can be valuable for certain applications. Thus, the orientation of an Airy beam structure was angularly switched by using a rotated phase-amplitude mask obtained with a series of computer-generated holograms that were applied to the SLM, eliminating the need for any mechanical motion device. As a result, we experimentally generated Airy beams with changeable curved directions. Our approach allows also for precise control over the trajectory of the beam, enabling applications that require dynamic steering.

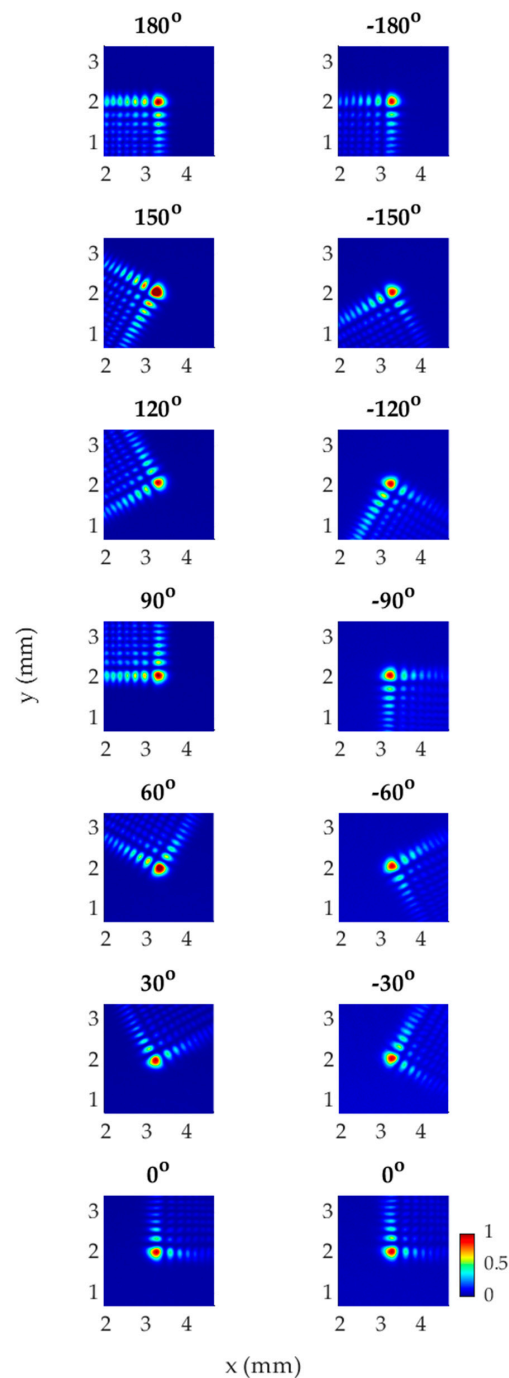


Figure 11. Generation of angle-adjustable optical Airy beams. The images show the intensity distributions for various Airy pattern orientation angles ranging from -180° to 180° in steps of 30° .

4. Conclusions

Airy beams were generated through direct phase and amplitude encoding by displaying holographic masks on a spatial light modulator. To create an Airy beam using a phase-only SLM, the desired phase pattern was first calculated using analytical methods. This phase pattern was then uploaded onto the SLM, which imposes the desired spatial phase modulation onto the incident laser beam. The original position of the generated Airy beam was controlled by manipulating the central position of the phase mask, eliminating the need for mechanical devices. By using a computer-controlled approach based on phase-amplitude encoding onto the phase-grating structure, we also experimentally generated Airy beams with changeable curved directions. Thus, we have shown how a spatial light modulator can be used as a versatile tool for direction control of Airy beams. Instead of manipulating an Airy beam by moving the optical components (e.g., lenses and apertures), we in situ generated holograms and manipulated the phase masks on the SLM in real time to change the direction of the Airy beam as needed. This allows for precise control over the trajectory of the beam, enabling applications that require dynamic steering. The presented approach can find applications in light sheet microscopy [15], providing an easy way of scanning the beam and also as a way to generate Airy beams without using a focusing lens, thus simplifying the setup and its alignment. The described method can be also useful for control of the beam routing and multiplexing [13]. Our approach makes it easy to shift the position of the Airy beam, which is useful for precise beam positioning and its direction adjustment in microsurgery [33]. The presented method effectively simplifies the experimental setup and provides also the advantage of using fewer optical elements, facilitating interdisciplinary and multidisciplinary scientific studies such as optical trapping, optical communication, biomedical imaging, etc., as it offers a versatile platform for dynamic generation and manipulation of Airy beams.

Author Contributions: Conceptualization, N.K., A.K., G.K. and A.A.K.; methodology, A.K., N.K., G.K. and A.A.K.; software, A.K., N.K. and A.A.K.; validation, A.K., N.K., J.S., A.A.K. and G.K.; formal analysis, A.K., A.A.K. and J.S.; investigation, A.K., N.K. and G.K.; resources, N.K. and A.K.; data curation, A.K. and N.K.; writing—original draft preparation, N.K. and A.A.K.; writing—review and editing, A.K., N.K., G.K., J.S., H.A.S. and A.A.K.; visualization, A.K. and N.K.; supervision, N.K., A.A.K. and H.A.S.; project administration, N.K. and A.K.; funding acquisition, N.K. and A.K. All authors have read and agreed to the published version of the manuscript.

Funding: This research was supported by Çanakkale Onsekiz Mart University, The Scientific Research Coordination Unit, project number: FBA-2021-3488. We also acknowledge TÜBİTAK-BİDEB for their financial support (grant numbers 2211C- 1649B032309573 for A.K., 2219-1059B192300488 for N.K., and 2219-1059B192302459 for G.K.).

Data Availability Statement: The original contributions presented in the study are included in the article, further inquiries can be directed to the corresponding author.

Acknowledgments: The authors would like to express their gratitude to TÜBİTAK, Çanakkale Onsekiz Mart University (ÇOMÜ) and Texas A&M University (TAMU) for their valuable support and contributions to this work. Finally, we extend our appreciation to the ÇOMÜ-Photonics Research and TAMU-SIBOR laboratory/facility for providing the necessary equipment and resources for this research.

Conflicts of Interest: The authors declare no conflicts of interest.

References

1. Durnin, J. Exact solutions for nondiffracting beams. I. The scalar theory. *J. Opt. Soc. Am. A* **1987**, *4*, 651–654. [[CrossRef](#)]
2. Durnin, J.; Miceli, J.J.; Eberly, J.H. Diffraction-free beams. *Phys. Rev. Lett.* **1987**, *58*, 1499–1501. [[CrossRef](#)]
3. Berry, M.V.; Balazs, N.L. Nonspreading wave packets. *Am. J. Phys.* **1979**, *47*, 264–267. [[CrossRef](#)]
4. Siviloglou, G.A.; Christodoulides, D.N. Accelerating finite energy Airy beams. *Opt. Lett.* **2007**, *32*, 979–981. [[CrossRef](#)]
5. Siviloglou, G.A.; Broky, J.; Dogariu, A.; Christodoulides, D.N. Observation of Accelerating Airy Beams. *Phys. Rev. Lett.* **2007**, *99*, 213901. [[CrossRef](#)] [[PubMed](#)]

6. Siviloglou, G.A.; Broky, J.; Dogariu, A.; Christodoulides, D.N. Ballistic dynamics of Airy beams. *Opt. Lett.* **2008**, *33*, 207–209. [[CrossRef](#)]
7. Bandres, M.A.; Rodríguez-Lara, B.M. Nondiffracting accelerating waves: Weber waves and parabolic momentum. *N. J. Phys.* **2013**, *15*, 013054. [[CrossRef](#)]
8. Broky, J.; Siviloglou, G.A.; Dogariu, A.; Christodoulides, D.N. Self-healing properties of optical Airy beams. *Opt. Express* **2008**, *16*, 12880–12891. [[CrossRef](#)]
9. Abdollahpour, D.; Sunstov, S.; Papazoglou, D.G.; Tzortzakis, S. Spatiotemporal Airy Light Bullets in the Linear and Nonlinear Regimes. *Phys. Rev. Lett.* **2010**, *105*, 253901. [[CrossRef](#)]
10. Chong, A.; Renninger, W.H.; Christodoulides, D.N.; Wise, F.W. Airy–Bessel wave packets as versatile linear light bullets. *Nat. Photonics* **2010**, *4*, 103–106. [[CrossRef](#)]
11. Panagiotopoulos, P.; Papazoglou, D.G.; Couairon, A.; Tzortzakis, S. Sharply autofocused ring-Airy beams transforming into non-linear intense light bullets. *Nat. Commun.* **2013**, *4*, 2622. [[CrossRef](#)] [[PubMed](#)]
12. Zhang, J.; Yang, X. Periodic abruptly autofocusing and autodefocusing behavior of circular Airy beams in parabolic optical potentials. *Opt. Commun.* **2018**, *420*, 163–167. [[CrossRef](#)]
13. Rose, P.; Diebel, F.; Boguslawski, M.; Denz, C. Airy beam induced optical routing. *Appl. Phys. Lett.* **2013**, *102*, 101101. [[CrossRef](#)]
14. Voloch-Bloch, N.; Lereah, Y.; Lilach, Y.; Gover, A.; Arie, A. Generation of electron Airy beams. *Nature* **2013**, *494*, 331–335. [[CrossRef](#)]
15. Vettenburg, T.; Dalgarno, H.I.C.; Nylk, J.; Coll-Lladó, C.; Ferrier, D.E.K.; Čížmár, T.; Gunn-Moore, F.J.; Dholakia, K. Light-sheet microscopy using an Airy beam. *Nat. Methods* **2014**, *11*, 541–544. [[CrossRef](#)] [[PubMed](#)]
16. Hsu, H.-C.; Vyas, S.; Wu, J.-C.; Huang, K.-Y.; Liao, H.-S.; Yeh, J.A.; Luo, Y. Volume holographic illuminator for Airy light-sheet microscopy. *Opt. Express* **2024**, *32*, 167–178. [[CrossRef](#)]
17. Li, H.; Wu, Z.; Yang, Z.; Zhanghao, K.; Xi, P.; Jin, D. Axially overlapped multi-focus light sheet with enlarged field of view. *Appl. Phys. Lett.* **2021**, *118*, 223701. [[CrossRef](#)]
18. Wang, J.; Hua, X.; Guo, C.; Liu, W.; Jia, S. Airy-beam tomographic microscopy. *Optica* **2020**, *7*, 790–793. [[CrossRef](#)]
19. Polynkin, P.; Kolesik, M.; Moloney, J.V.; Siviloglou, G.A.; Christodoulides, D.N. Curved Plasma Channel Generation Using Ultraintense Airy Beams. *Science* **2009**, *324*, 229–232. [[CrossRef](#)]
20. Lin, Z.; Guo, X.; Tu, J.; Ma, Q.; Wu, J.; Zhang, D. Acoustic non-diffracting Airy beam. *J. Appl. Phys.* **2015**, *117*, 104503. [[CrossRef](#)]
21. Baumgartl, J.; Mazilu, M.; Dholakia, K. Optically mediated particle clearing using Airy wavepackets. *Nat. Photonics* **2008**, *2*, 675–678. [[CrossRef](#)]
22. Zheng, Z.; Zhang, B.-F.; Chen, H.; Ding, J.; Wang, H.-T. Optical trapping with focused Airy beams. *Appl. Opt.* **2011**, *50*, 43–49. [[CrossRef](#)] [[PubMed](#)]
23. Efremidis, N.K.; Paltoglou, V.; von Klitzing, W. Accelerating and abruptly autofocusing matter waves. *Phys. Rev. A* **2013**, *87*, 043637. [[CrossRef](#)]
24. Schneider, T.; Serga, A.A.; Chumak, A.V.; Sandweg, C.W.; Trudel, S.; Wolff, S.; Kostylev, M.P.; Tiberkevich, V.S.; Slavin, A.N.; Hillebrands, B. Nondiffractive Subwavelength Wave Beams in a Medium with Externally Controlled Anisotropy. *Phys. Rev. Lett.* **2010**, *104*, 197203. [[CrossRef](#)] [[PubMed](#)]
25. Polynkin, P.; Kolesik, M.; Moloney, J. Filamentation of Femtosecond Laser Airy Beams in Water. *Phys. Rev. Lett.* **2009**, *103*, 123902. [[CrossRef](#)]
26. Wiersma, N.; Marsal, N.; Sciamanna, M.; Wolfersberger, D. Spatiotemporal dynamics of counterpropagating Airy beams. *Sci. Rep.* **2015**, *5*, 13463. [[CrossRef](#)]
27. Mitri, F.G. Airy acoustical-sheet spinner tweezers. *J. Appl. Phys.* **2016**, *120*, 104901. [[CrossRef](#)]
28. Mitri, F.G. Acoustics of finite asymmetric exotic beams: Examples of Airy and fractional Bessel beams. *J. Appl. Phys.* **2017**, *122*, 224903. [[CrossRef](#)]
29. Piksarv, P.; Marti, D.; Le, T.; Unterhuber, A.; Forbes, L.H.; Andrews, M.R.; Stingl, A.; Drexler, W.; Andersen, P.E.; Dholakia, K. Integrated single- and two-photon light sheet microscopy using accelerating beams. *Sci. Rep.* **2017**, *7*, 1435. [[CrossRef](#)]
30. Nylk, J.; McCluskey, K.; Preciado, M.A.; Mazilu, M.; Yang, Z.; Gunn-Moore, F.J.; Aggarwal, S.; Tello, J.A.; Ferrier, D.E.K.; Dholakia, K. Light-sheet microscopy with attenuation-compensated propagation-invariant beams. *Sci. Adv.* **2018**, *4*, eaar4817. [[CrossRef](#)]
31. Veetikazhy, M.; Nylk, J.; Gasparoli, F.; Escobet-Montalbán, A.; Hansen, A.K.; Marti, D.; Andersen, P.E.; Dholakia, K. Multi-photon attenuation-compensated light-sheet fluorescence microscopy. *Sci. Rep.* **2020**, *10*, 8090. [[CrossRef](#)] [[PubMed](#)]
32. Efremidis, N.K.; Christodoulides, D.N. Abruptly autofocusing waves. *Opt. Lett.* **2010**, *35*, 4045–4047. [[CrossRef](#)] [[PubMed](#)]
33. Papazoglou, D.G.; Efremidis, N.K.; Christodoulides, D.N.; Tzortzakis, S. Observation of abruptly autofocusing waves. *Opt. Lett.* **2011**, *36*, 1842–1844. [[CrossRef](#)] [[PubMed](#)]
34. Yalizay, B.; Soyulu, B.; Akturk, S. Optical element for generation of accelerating Airy beams. *J. Opt. Soc. Am. A* **2010**, *27*, 2344–2346. [[CrossRef](#)]
35. Papazoglou, D.G.; Sunstov, S.; Abdollahpour, D.; Tzortzakis, S. Tunable intense Airy beams and tailored femtosecond laser filaments. *Phys. Rev. A* **2010**, *81*, 061807. [[CrossRef](#)]
36. Dai, H.T.; Sun, X.W.; Luo, D.; Liu, Y.J. Airy beams generated by a binary phase element made of polymer-dispersed liquid crystals. *Opt. Express* **2009**, *17*, 19365–19370. [[CrossRef](#)]

37. Liu, Y.; Chen, W.; Tang, J.; Xu, X.; Chen, P.; Ma, C.-Q.; Zhang, W.; Wei, B.-Y.; Ming, Y.; Cui, G.-X.; et al. Switchable Second-Harmonic Generation of Airy Beam and Airy Vortex Beam. *Adv. Opt. Mater.* **2021**, *9*, 2001776. [[CrossRef](#)]
38. Wu, D.; Zhang, Z.; Wang, C.; Zhang, L.; Xu, L.; Wei, D.; Xiong, W.; Li, J.; Hu, Y.; Chu, J.; et al. Generation of nonlinear Airy beams with switchable acceleration direction. *J. Opt.* **2023**, *25*, 07LT01. [[CrossRef](#)]
39. Fan, Q.; Zhu, W.; Liang, Y.; Huo, P.; Zhang, C.; Agrawal, A.; Huang, K.; Luo, X.; Lu, Y.; Qiu, C.; et al. Broadband Generation of Photonic Spin-Controlled Arbitrary Accelerating Light Beams in the Visible. *Nano Lett.* **2019**, *19*, 1158–1165. [[CrossRef](#)]
40. Ellenbogen, T.; Voloch-Bloch, N.; Ganany-Padowicz, A.; Arie, A. Nonlinear generation and manipulation of Airy beams. *Nat. Photonics* **2009**, *3*, 395–398. [[CrossRef](#)]
41. Trajtenberg-Mills, S.; Juwiler, I.; Arie, A. Generation of second-harmonic beams with switchable curved trajectories. *Optica* **2017**, *4*, 153–156. [[CrossRef](#)]
42. Dolev, I.; Ellenbogen, T.; Arie, A. Switching the acceleration direction of Airy beams by a nonlinear optical process. *Opt. Lett.* **2010**, *35*, 1581–1583. [[CrossRef](#)] [[PubMed](#)]
43. Zhang, Y.; Belić, M.R.; Zhang, L.; Zhong, W.; Zhu, D.; Wang, R.; Zhang, Y. Periodic inversion and phase transition of finite energy Airy beams in a medium with parabolic potential. *Opt. Express* **2015**, *23*, 10467–10480. [[CrossRef](#)] [[PubMed](#)]
44. Davis, J.A.; Cottrell, D.M.; Campos, J.; Yzuel, M.J.; Moreno, I. Encoding amplitude information onto phase-only filters. *Appl. Opt.* **1999**, *38*, 5004–5013. [[CrossRef](#)]
45. Bentley, J.B.; Davis, J.A.; Bandres, M.A.; Gutiérrez-Vega, J.C. Generation of helical Ince-Gaussian beams with a liquid-crystal display. *Opt. Lett.* **2006**, *31*, 649–651. [[CrossRef](#)]
46. Strohaber, J. *Intense-Field Ionization of Atoms and Molecules: Spatially Resolved Ion Detection and Ultrashort Optical Vortices*; ETD collection for University of Nebraska-Lincoln; University of Nebraska-Lincoln: Lincoln, NE, USA, 2008.
47. Strohaber, J.; Kaya, G.; Kaya, N.; Hart, N.; Kolomenskii, A.A.; Paulus, G.G.; Schuessler, H.A. In situ tomography of femtosecond optical beams with a holographic knife-edge. *Opt. Express* **2011**, *19*, 14321–14334. [[CrossRef](#)]

Disclaimer/Publisher’s Note: The statements, opinions and data contained in all publications are solely those of the individual author(s) and contributor(s) and not of MDPI and/or the editor(s). MDPI and/or the editor(s) disclaim responsibility for any injury to people or property resulting from any ideas, methods, instructions or products referred to in the content.